Synthesis, structural and electrochemical characterizations of the sol–gel birnessite $MnO_{1.84} \cdot 0.6H_2O$

S. Franger[a], S. Bach[a,*], J. Farcy[a], J.-P. Pereira-Ramos[a], N. Baffier[b]

[a]*LECSO, CNRS UMR 7582, Laboratoire d'Electrochimie, Catalyse et Synthese Organique, Cen Natl de la Recherche Scie.,
2 a 8, rue Henri-Dunant, B.P. 28, 94320 Thiais, France*
[b]*LCAES, CNRS UMR 7574, 11 rue Pierre et Marie Curie, 75231 Paris, France*

Abstract

The electrochemical features of the sol–gel birnessite $MnO_{1.84} \cdot 0.6H_2O$ are reported here in terms of OCV data, cycling behavior kinetics of Li transport in the oxide.

We have confirmed that the sol–gel birnessite remains one of the best manganese oxides as rechargeable cathodic materials with an initial specific capacity of 270 mAh g^{-1} due to the high amount of Mn(IV). However, from a practical viewpoint, this hydrated compound has been proved to exhibit an important and constant capacity fading in the potential window 4.2–2 V associated with a strong disordering process. The ac impedance measurements have proved this behavior was mainly due to an increase of the cathode impedance and a strong decrease in kinetics of Li transport in the oxide.

Such a phenomenon can be overcome when the Co-doped form $Co_{0.15}Mn_{0.85}O_{1.84} \cdot 0.6H_2O$ is used. In that case, a constant capacity as high as 170 mAh g^{-1} can be maintained over more than 50 cycles with no change in the electrochemical behavior of the Co-doped sample.

This clearly shows that stable capacity can be expected even from a hydrated oxide network. © 2002 Elsevier Science B.V. All rights reserved.

Keywords: Intercalation compounds; Sol–gel; Birnessite compound

1. Introduction

Among the lithium transition metal oxide intercalation compounds, MnO_2-based oxides have attracted a great deal of research because of its economical advantages [1–3]. For example, heat-treated γ-MnO_2 [4,5], consisting of irregular structural intergrowth between pyrolusite and ramsdellite units, or lithiated MnO_2 electrodes, referred as CDMO, interpreted in terms of a composite structure containing domains of γ-MnO_2 and Li_2MnO_3 [6–8] have been used in rechargeable 3 V lithium batteries. In more recent developments, the spinel system $Li_xMn_2O_4$ $(0 < x < 1)$ has found application in rechargeable 4 V lithium-ion cells [9–11]. An important problem prohibiting them from use as a cathode for lithium batteries is their undesirable capacity fading phenomena on prolonged cycling in the three or in the 4 V region [12–18]. In these studies, the effect of crystalline structure, the morphology of the powders, oxygen stoichiometry or partial substitution of manganese with

other elements such as Ni, Co or Cr [3,19] have been investigated to improve capacity retention and specific capacity.

In recent years, several low temperature techniques such as sol–gel and precipitation processes have been developed for preparing new manganese oxides. The sol–gel process in aqueous solutions is based on hydrolysis and condensation of metal ions [20,21]. This kind of synthesis allows a better control of the morphology and texture of solid particles. In previous work [22–24], we have pointed out the interest of this technique for the synthesis of new cathodic intercalation materials for secondary Li cells, especially V_2O_5 and MnO_2 based compounds [25]. One of most promising compounds has been found to be a layered manganese oxide named birnessite of formula $MnO_{1.84} \cdot 0.6H_2O$ [26,27]. From chronopotentiometric and voltammetric studies, electrochemical Li insertion in this compound has been shown to occur reversibly in the potential range 4.4–2 V versus Li/Li$^+$ with a maximum faradaic balance to 0.8 F mol^{-1} of oxide [26,27]. In spite of these attractive properties, a significant capacity decay takes place during cycling since only 75% of the initial capacity (230 mAh g^{-1}) is reached after the fiftieth cycle [26,27].

* Corresponding author. Tel.: +33-1-49-78-11-43;
fax: +33-1-4978-1323.
E-mail address: bach@glvt-cnrs.fr (S. Bach).

Table 1
Slope of the equilibrium potential composition curve as a function of x in the compound $Li_xMnO_{1.84} \cdot 0.6H_2O$

Insertion rate x	Slope dE/dx (V mol^{-1})
0.025	−7.00
0.075	−4.00
0.01	−3.60
0.15	−3.00
0.2	−2.50
0.25	−2.00
0.3	−1.50
0.35	−1.00
0.4	−0.84
0.45	−0.60
0.5	−0.95
0.55	−1.00
0.6	−1.14
0.65	−2.00
0.7	−2.12
0.75	−2.50

In order to understand and to solve this capacity fading we have undertaken a deeper insight into the electrochemical behavior of birnessite. The kinetics of the lithium transport is investigated in $Li_xMnO_{1.84} \cdot 0.6H_2O$ through the determination of the chemical diffusion coefficients of lithium ions using ac impedance measurements and the pulse relaxation technique [28]. The results are discussed in relation with chemical, physical and structural properties (Table 1).

2. Experimental

The mean oxidation state of manganese (Z_{Mn}) was determined by a chemical titration using ferrous ammonium sulphate and potassium permanganate with an accuracy of $\pm 2\%$ [29]; the powder sample is dissolved in an aqueous solution containing 50% (vol.) concentrated H_2SO_4 and an excess of ferrous ammonium sulphate. During the dissolution of the powder, the Mn(IV) ions from the sample are reacted with Fe(II) and finally the excess of Fe^{2+} ions are titrated with an aqueous solution of MnO_4^-.

Chemical composition of the compound was made by elemental analysis using the ICP–MS technic (Inductive Coupled Plasma–Mass Spectrometry). XRD experiment was performed with a Philips D 5000 diffractometer using the Co Kα radiation ($\lambda = 1.7889$ Å). The morphology and the grain size of the sample were performed with a Philips XL 30 scanning electron microscope. The thermal analysis (TGA/DSC) was made with a Netzsch STA 409 analyzer.

Electrochemical studies were carried out in Swagelok® type two electrodes cells (Fig. 1) for the galvanostatic measurements and cycling tests. Open circuit voltage and ac impedance spectroscopy experiments were performed in classical three electrodes cell. The working electrode consisted of a stainless steel grid with a geometric area of 1 cm^2 on which the cathodic material was pressed. The cathode was made by a mixture of active material (80 wt.%), graphite (7.5 wt.%), acetylene black (7.5 wt.%) and teflon as binder
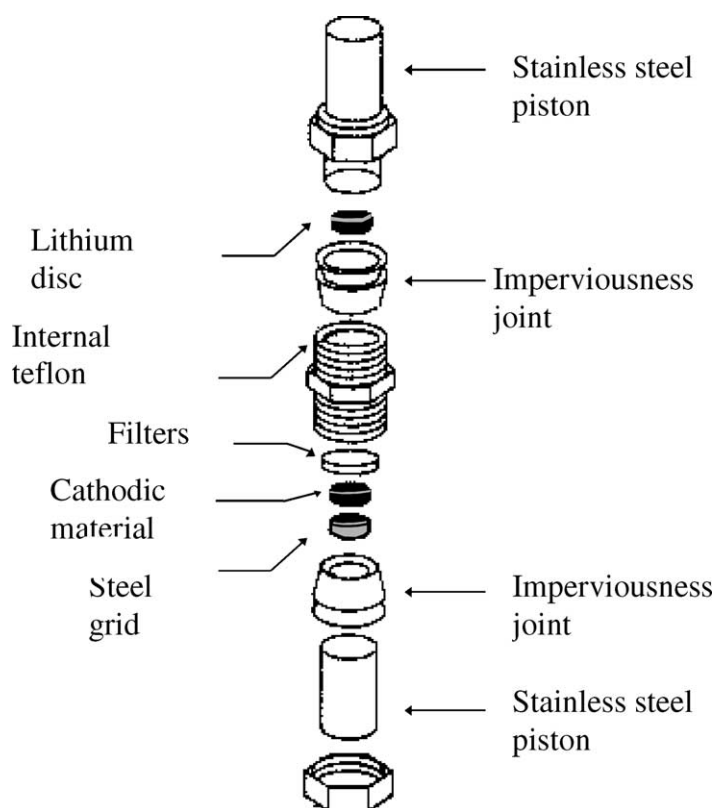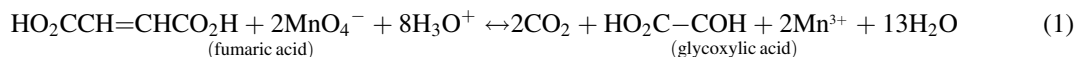

Fig. 1. Swagelok® type two electrodes cell.

agent (5 wt.%). The film is obtained, in 10 min, by mixing the oxide powder, carbon and teflon. The counter and reference electrodes were respectively platinum and lithium wires in separate compartments. The electrolyte used was 1 mol l^{-1} LiClO$_4$, dried under vacuum at 170 °C for 15 h, dissolved in twice distilled propylene carbonate obtained from Fluka$^{®}$.

Galvanostatic measurements were made with a MacPileII apparatus. The working composition was changed by coulometric titration. Equilibrium was considered to be reached when the open circuit voltage remained stable (<1 mV for 24 h).

Impedance measurements were made, in the frequency range 4×10^4 to 10^{-3} Hz, with an E.G.G. 273A apparatus connected with an E.G.G. 5208 two phase lock, in an analyser drived by an IBM computer. The excitation signal was 15 mV, peak to peak. The equilibrium potential was considered to be reached when the drift in open circuit voltage remained less than 0.2 mV for 1 h.
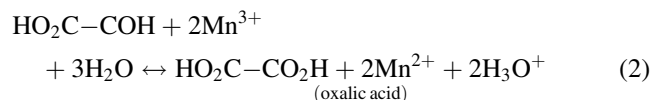
2.1. Recall on the sol–gel synthesis

The manganese dioxide, MnO$_2$ can be easily prepared via reduction of an alkaline permanganate salt by an organic acid such as the fumaric acid [23]. The associated reaction is:

$$\underset{\text{(fumaric acid)}}{HO_2CCH{=}CHCO_2H} + 2MnO_4^- + 8H_3O^+ \leftrightarrow 2CO_2 + \underset{\text{(glycoxylic acid)}}{HO_2C{-}COH} + 2Mn^{3+} + 13H_2O \qquad (1)$$

Under basic conditions (pH > 7), the aldehyde function can be oxidized as following:

$$HO_2C{-}COH + 2Mn^{3+}$$
$$+ 3H_2O \leftrightarrow \underset{\text{(oxalic acid)}}{HO_2C{-}CO_2H} + 2Mn^{2+} + 2H_3O^+ \qquad (2)$$

With an excess of MnO$_4^-$ ions, the Mn(II) formed are not stable and gives MnO$_2$ rapidly. This is experimentally observed for an initial ratio MnO$_4^-$/C$_4$H$_4$O$_4$ = 3:

$$3C_4H_4O_4 + 10AMnO_4 \leftrightarrow [10MnO_2 + 3(ACO_2)_2$$
$$+ 4AOH + 4H_2O]_{gel} + 6CO_2 \qquad (3)$$

NaMnO$_4$ KMnO$_4$

Reduction with fumaric acid

Monolithic gels (in 5 – 6 minutes) with manganese IV

Heat - treatment → Formation
of ternary oxides A$_x$MnO$_2$ (A = Na, K)

α-Na$_{0.7}$MnO$_2$ 600°C   K$_{0.25}$MnO$_2$

Acidic treatment → Equivalent
to a chemical oxidation

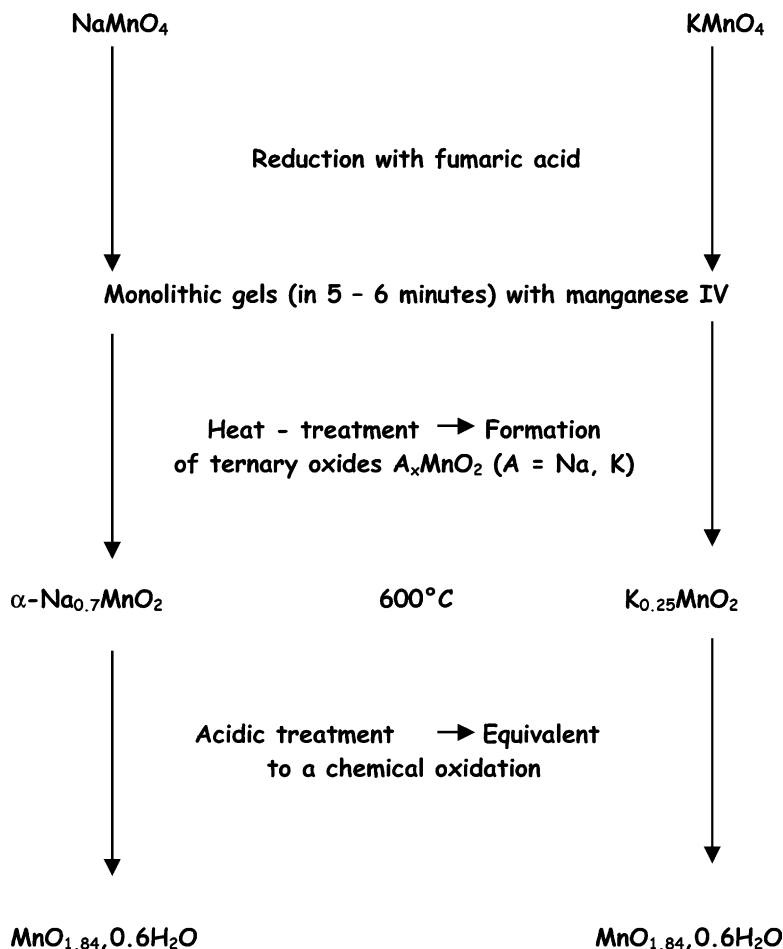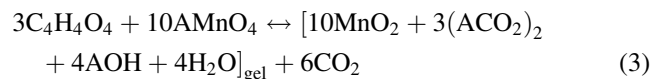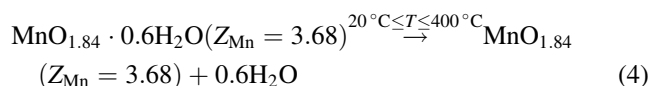MnO$_{1.84}$,0.6H$_2$O   MnO$_{1.84}$,0.6H$_2$O

Fig. 2. Schematic synthesis of the sol–gel birnessite.

A dark brown gel is obtained in approximately 15 min. The natural dehydratation at room temperature of this gel gives the xerogel which contains the degradation products of the fumaric acid oxidation (alkaline oxalate and hydroxide). The xerogel is then heat-treated at 600 °C in air for 10 h. The resulting product is a ternary oxide α-$Na_{0.7}MnO_2$ ($Z_{Mn} = 3.3$, α-$Na_{0.7}[Mn_{0.7}{}^{3+}Mn_{0.3}{}^{4+}]O_2$). When a potassium permanganate aqueous solution is used instead of $NaMnO_4$, the layered ternary oxide $K_{0.25}MnO_2$ ($Z_{Mn} = 3.75$, $K_{0.25}[Mn_{0.25}{}^{3+}Mn_{0.75}{}^{4+}]O_2$) is finally obtained.
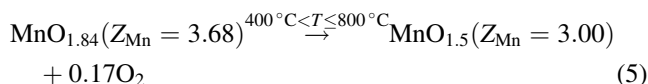
An acidic treatment (H_2SO_4 1 mol l^{-1}) performed on trivalent manganese oxide phases, provokes the release into the solution of alkali ions followed by disproparnation of the Mn^{3+} into soluble Mn^{2+} and insoluble Mn^{4+} ions. Thus, in this case, the solid network progressively transforms into birnessite compound $MnO_{1.84} \cdot 0.6H_2O$ ($Z_{Mn} = 3.68$, $[Mn_{0.16}{}^{2+}Mn_{0.84}{}^{4+}]O_{1.84} \cdot 0.6H_2O$) (Fig. 2).

3. Results and discussion

The simultaneous thermal analysis (TGA/DSC) of the sol–gel birnessite, $Z_{Mn} = 3.68$ (Fig. 3), performed between room temperature to 800 °C with a flow rate of 10 °C min^{-1}, shows a total weight loss of 18%. The first large endothermic peak at 190 °C corresponds to a weight loss of 11% and is associated with the departure of all the water molecules from the compound with no variation of the oxidation state. A last endothermic peak appears at 540 °C with a weight loss of about seven percent corresponding to structural transformation accompanied by changes in Z_{Mn}. Indeed, above 500 °C, a decomposition reaction takes place with oxygen departure leading to the formation of Mn_2O_3. From these experimental results and the measured oxidation state of manganese in birnessite, $Z_{Mn} = 3.68$, the successive weight losses can be described by the following two equations:

$$MnO_{1.84} \cdot 0.6H_2O(Z_{Mn} = 3.68) \overset{20\,°C \leq T \leq 400\,°C}{\rightarrow} MnO_{1.84}$$
$$(Z_{Mn} = 3.68) + 0.6H_2O \tag{4}$$

$$\Delta M_{theoretical} = -11.34\% \quad \Delta M_{observed} = -11.00\%$$

$$MnO_{1.84}(Z_{Mn} = 3.68) \overset{400\,°C < T \leq 800\,°C}{\rightarrow} MnO_{1.5}(Z_{Mn} = 3.00)$$
$$+ 0.17O_2 \tag{5}$$

$$\Delta M_{theoretical} = -6.44\% \quad \Delta M_{observed} = -7.00\%$$

The X-Ray diffraction pattern of the $MnO_{1.84} \cdot 0.6H_2O$ is shown in Fig. 4a. The most intensive lines correspond to the (0 0 1) planes. The structure of the birnessite can be described as a lamellar phase of hexagonal symmetry ($P\bar{3}m1$) with the following cell parameters: $a = 2.84$ Å, $c = 7.24$ Å. From the observation of Fig. 4a, it is apparent that the sol–gel compound exhibits an important preferred orientation since only the (0 0 1) and (0 0 2) peaks appear with noticeable intensities. This indicates a stacking of the layers parallel to the (a, b) plane over large domains.

The SEM micrographs (Fig. 5a and b) performed on the birnessite show that the sol–gel process gives the advantage of homogeneity, both, in terms of particle size and morphology. The mean grain size ($\varnothing$) observed is about 4 μm.

There is a wide variety of layered Mn(IV) oxides, like birnessite [26,30–32], 2D Ranceite [33], or buserite [34,35], which differ by the interlayer distance, the ion-exchange capacity, the interlayer cation content, the manganese oxidation state, the IR spectrum. Another way of synthesis for birnessite compound (that we called "classical birnessite") is the Stähli method [30] consisting in an oxidation of $Mn(OH)_2$ with O_2 or Cl_2 in NaOH which leads to the Na-birnessite with the formula $Na_4Mn_{14}O_{27} \cdot 9H_2O$ or $Na_{0.32}MnO_2 \cdot 0.67H_2O$ and to the free sodium compound with the following formula $Mn_7O_{13} \cdot 5H_2O$ or $MnO_{1.86} \cdot 0.7H_2O$ close to the formula of our compound. Depending on the synthesis way, a combination of Mn(IV)/Mn(III) or Mn(IV)/Mn(II) can be found in birnessite. For example, the mean oxidation state of manganese in our material and the classical birnessite (prepared from Stähli method) varies in the range $3.6 < Z_{Mn} < 3.8$. However, we have shown that in our case [26,27], we have a mixture of Mn(IV) and Mn(II) while a combination of Mn(IV) and Mn(III) is found for the
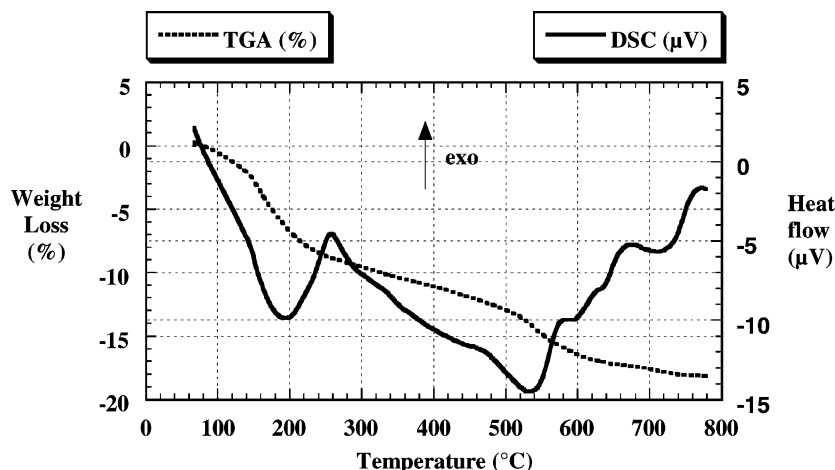

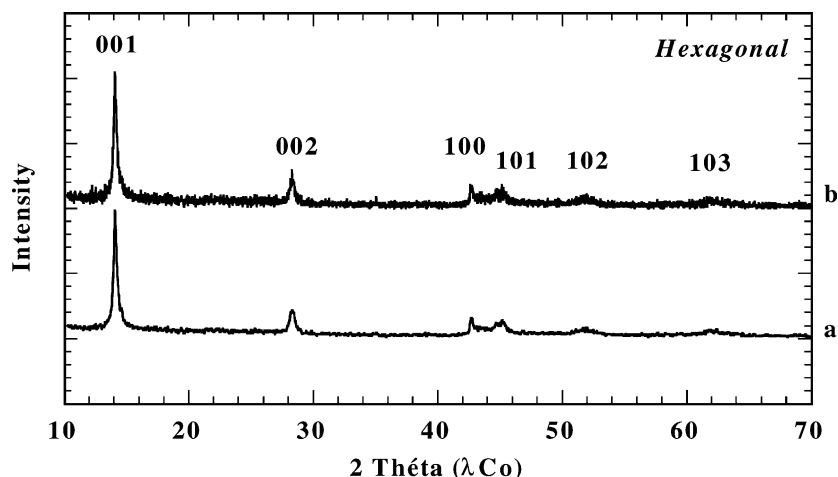Fig. 3. TGA/DSC curves of the sol–gel birnessite between RT and 800 °C at 0 °C min^{-1}

Fig. 4. XRD diffraction pattern of (a) the sol–gel birnessite and (b) the sol–gel Co-birnessite (l Co Kα).

classical birnessite. In both cases, the precise determination of the structure of material has never been performed. Nevertheless, these phases are known to exhibit an hexagonal or monoclinic symmetry, one like the layered CdI_2 type structure consisting of single sheet of water molecules between layers of edge-sharing $[MnO_6]$ octahedra with

Mn^{2+} located between the water layer and oxygen of the $[MnO_6]$ layer.

The sequence on the c-axis is then:

$$O-Mn(IV)-O-Mn(III)^+ \text{ or } (II)^*-H_2O-Mn(III)^+ \text{ or } (II)^*$$
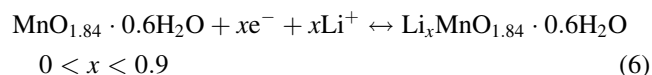$$-O-Mn(IV)-O$$
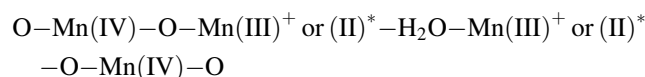
$(+)$, classical birnessite; $(^*)$, our compound.

The orthogonal distance between two consecutive slabs of $[MnO_6]$ is close to 7.24 Å (Fig. 6).

4. Electrochemical characterization

The electrochemical insertion of the lithium ions into the sol–gel $MnO_{1.84} \cdot 0.6H_2O$ structure can be written as following:

$$MnO_{1.84} \cdot 0.6H_2O + xe^- + xLi^+ \leftrightarrow Li_xMnO_{1.84} \cdot 0.6H_2O$$
$$0 < x < 0.9 \qquad (6)$$

x represents the number of mole of electrons per mole of oxide and also corresponds to the lithium content intercalated into the host lattice.

A typical discharge–charge profile of the sol–gel birnessite performed at low rate ($C/20$) is reported in Fig. 7a.

The electrochemical insertion of lithium ions is responsible for a continuous decrease of the working potential from 4.2 to 2 V (Fig. 7a); a first insertion step takes place between 4.5 and 3 V corresponding to a Li uptake of 0.4. The working potential then changes more slowly with the Li content to reach 2.5 V for $x = 0.75$–0.8. The total faradaic balance is equal to 0.8 F mol^{-1} of oxide and corresponds to the reduction of almost all the Mn(IV) ions available in the birnessite.

The reversibility aspect of the electrochemical insertion reaction of the lithium ions into $MnO_{1.84} \cdot 0.6H_2O$ has been considered from the OCV data reported in Fig. 7b and XRD experiments. Even when from XRD data, we have shown the initial structure is completely restored after a
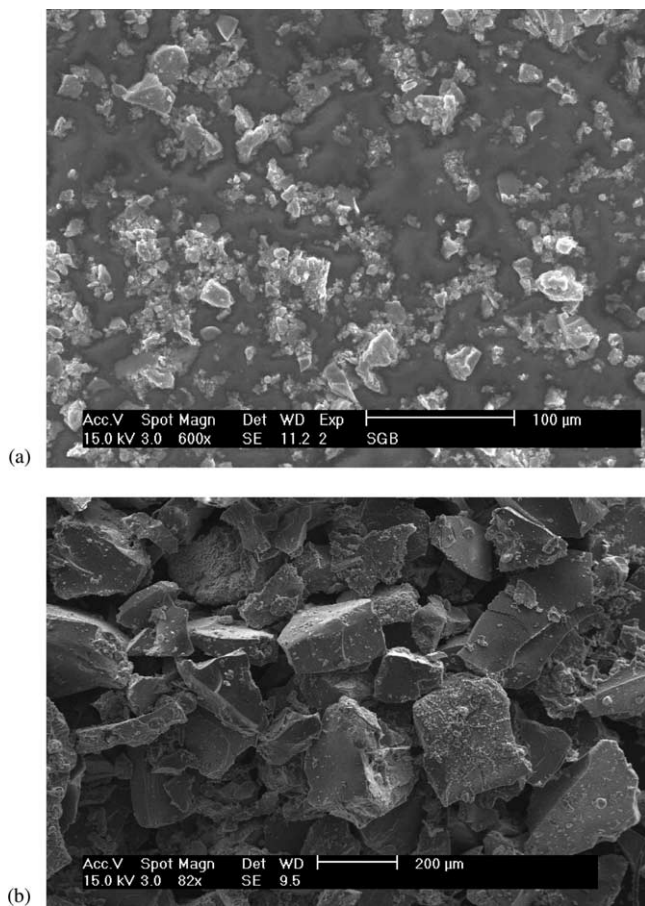

(a)

(b)

Fig. 5. Scanning electron micrographs of (a) $MnO_{1.84} \cdot 0.6H_2O$ and (b) $Mn_{0.85}Co_{0.15}O_{1.84} \cdot 0.6H_2O$.

Layered hexagonal structure of the birnessite
$MnO_{1.84}, 0.6H_2O$
($a = 2.84$ Å, $c = 7.24$ Å)

Octahedra [MnO_6] from the layers of Mn^{4+} ions
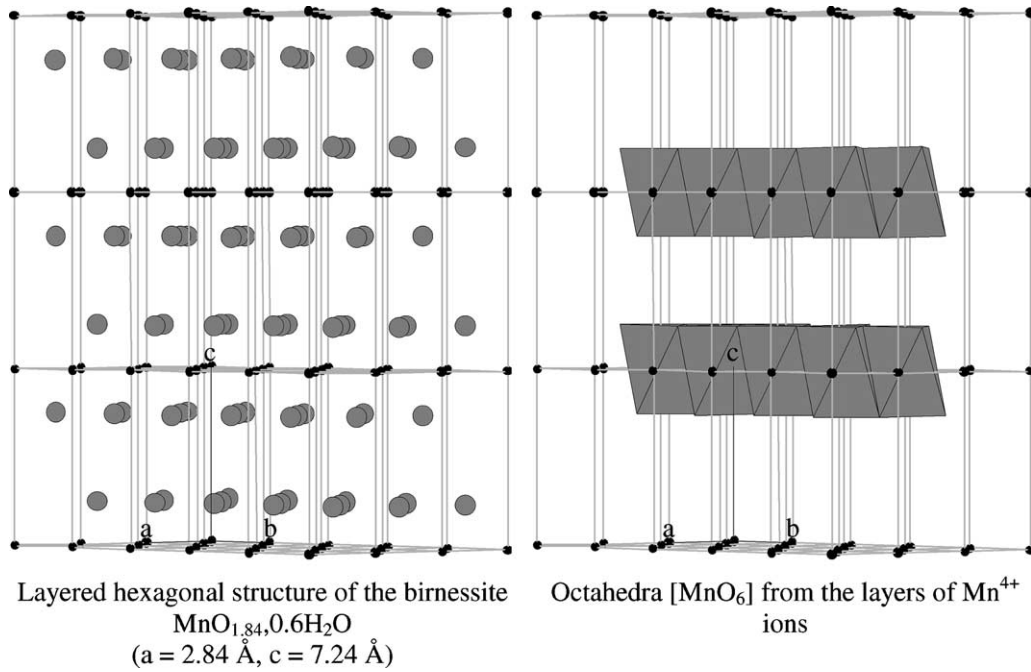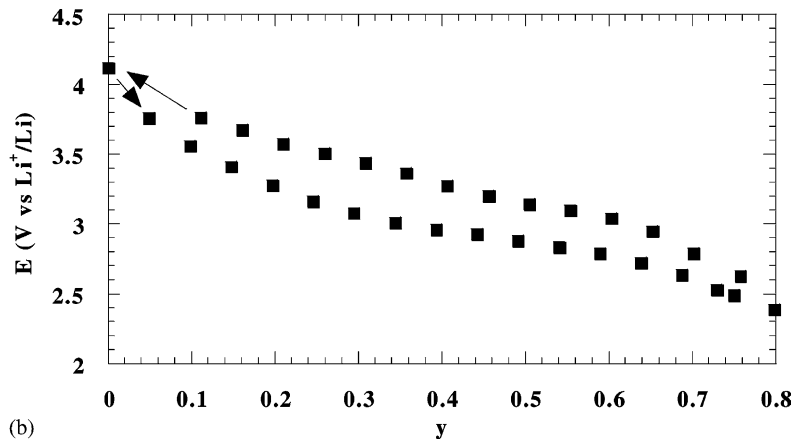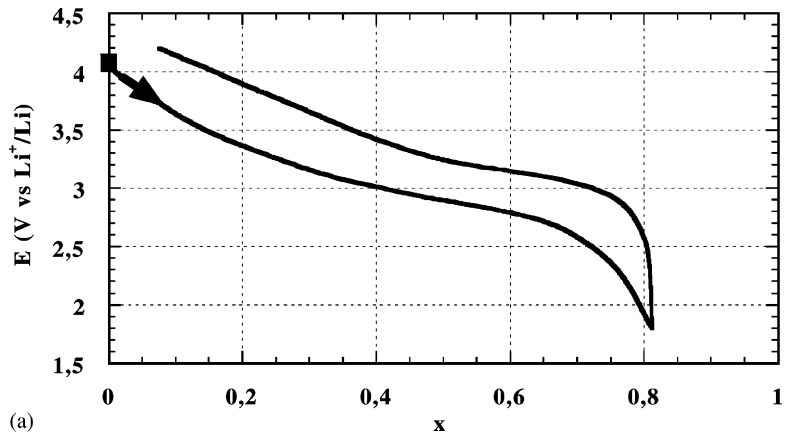
Fig. 6. Structure of the sol–gel birnessite.

Fig. 7. (a) Galvanostatic curve at $C/20$ between 4.2 and 1.8 V obtained in Swagelok®-LiClO$_4$ 1 mol l^{-1}/PC. (b) OCV curve of the sol–gel birnessite (equilibrium condition: dE/dt <1 mV h^{-1}) between 4.2 and 2.5 V.
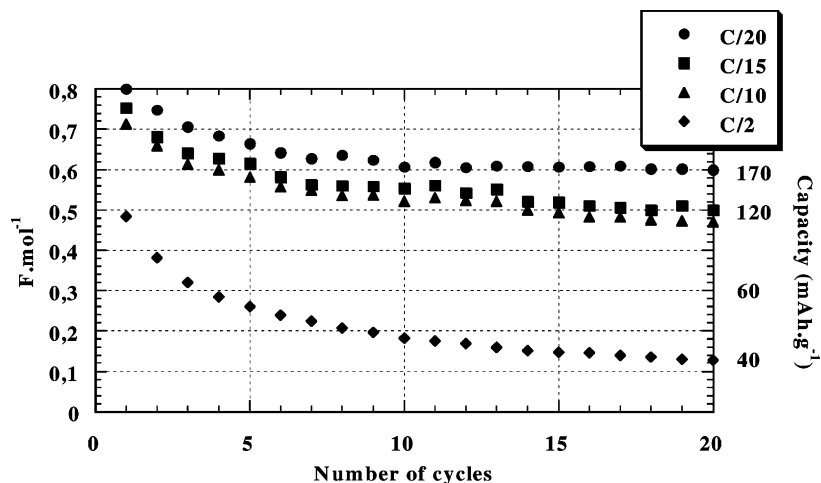
Fig. 8. Evolution of the faradaic capacity with the number of cycles and in function of the charge–discharge rate.

discharge–charge cycle [26], neither the OCV curve obtained for insertion–extraction reaction, neither the discharge–charge curves completely superimposed showing the starting material, is not completely recovered after the first Li insertion–extraction cycle.

Fig. 8 summarizes the evolution of the specific capacity of sol–gel birnessite as a function of the number of cycles with different rates of charge–discharge (from $C/20$ to $C/2$) in the voltage range 4.2–2 V. For the lowest rate, the capacity rapidly decreases from 230 mAh g^{-1} to stabilize at around 170 mAh g^{-1} after 10 cycles. At the highest rate, the capacity always decreases. At $C/15$ and $C/10$ rates the stabilization of the specific capacity takes place around 130–150 mAh g^{-1} after 10 cycles. In a few words, it comes out that the rechargeability of the sol–gel birnessite is highly sensitive to the current density applied, meaning that the kinetics of Li^{+} transport mainly governs the rechargeability and the cycle life of the material.

In order to quantify the lithium diffusion coefficient in the sol–gel birnessite, we have performed two types of electrochemical measurements. One was ac impedance spectroscopy, the other was the current pulse relaxation technique (CPRT) developed by Basu and Worrel [28]. The first one consists to collect the current response during a sinusoidal potentiostatic signal in order to determine the impedance (Z) of the system, whereas for the second, it requires a continuous galvanostatic pertubation and the potentiometric response is analyzed after interrupting the current.

By analogy with solid solutions of metal and alloys, the electrochemical lithium insertion–extraction process into birnessite may be regarded as a simple dissolution reaction, the kinetics of which is limited by the Li diffusion in the host material. If the time constants of the different processes are well separated [36], the impedance of the system reported in the complex plane (ReZ versus ImZ) consists of (i) a semicircle centered on the real axis at high frequencies from which ohmic resistance (R_0), double layer capacitance, and the charge transfer resistance (R_{CT}) may be deduced

(and consequently the exchange current density $j_0 = RT/nFSR_{CT}$), (ii) a straight line with an angle of 45° with the real axis corresponding to the Warburg impedance $Z_W = A\omega^{-1/2} - jA\omega^{-1/2}$ (semi-infinite diffusion) at low frequencies. At lower frequencies, the phase angle increases due to finite length (L) diffusion process and a limiting resistance R_L is obtained ($R = R_0 + R_{CT} + R_L$).

A typical ac impedance diagram [36], obtained for Li$_{0.2}$MnO$_{1.84}$·0.6H$_2$O is reported in Fig. 9. The diagram presents three regions. A semicircle is evidenced in the high-medium frequency range and corresponds to the charge transfer (with a characteristic frequency $f^* \sim 10^2$ Hz). The low frequency response is characterized by a straight line with a phase angle of 45° from the real axis corresponding to the Warburg impedance from which the numerical values of D_{Li} are calculated using Eq. (7):

$$D_{Li} = \left[\frac{V_M}{F\sqrt{2}} \left(\frac{dE}{dx} \right)_x \frac{1}{AS} \right]^2 \qquad (7)$$

where, V_M is the molar volume of the compound (=25 cm^3 mol^{-1}), S the active surface area of the electrode (cm^2), $(dE/dx)_x$ the slope at fixed x of the equilibrium potential composition curve (Fig. 7b and Table 2).

This region corresponds to a frequency range where the kinetics of the system is almost entirely limited by the rate of the chemical diffusional process in the host material. Its position in frequency significantly depends on the lithium content in birnessite. For instance, the frequency range of the Warburg region changes from 10^{-1} to 10^{-2} Hz for $x = 0.2$ (Fig. 9a) to 1×10^{-2} to 3×10^{-3} Hz for $x = 0.6$ (Fig. 9b). This qualitatively indicates a decrease of the chemical Li diffusion coefficient D_{Li} when x increases while the kinetics of the charge transfer does not change. The D_{Li} values determined from ac impedance experiments are reported in Fig. 11.

Finally, at lower frequencies (10^{-3} to 10^{-4} Hz) the 45° line begins to give way to a vertical line (i.e. the phase angle is increasing) corresponding to the finite diffusion process.
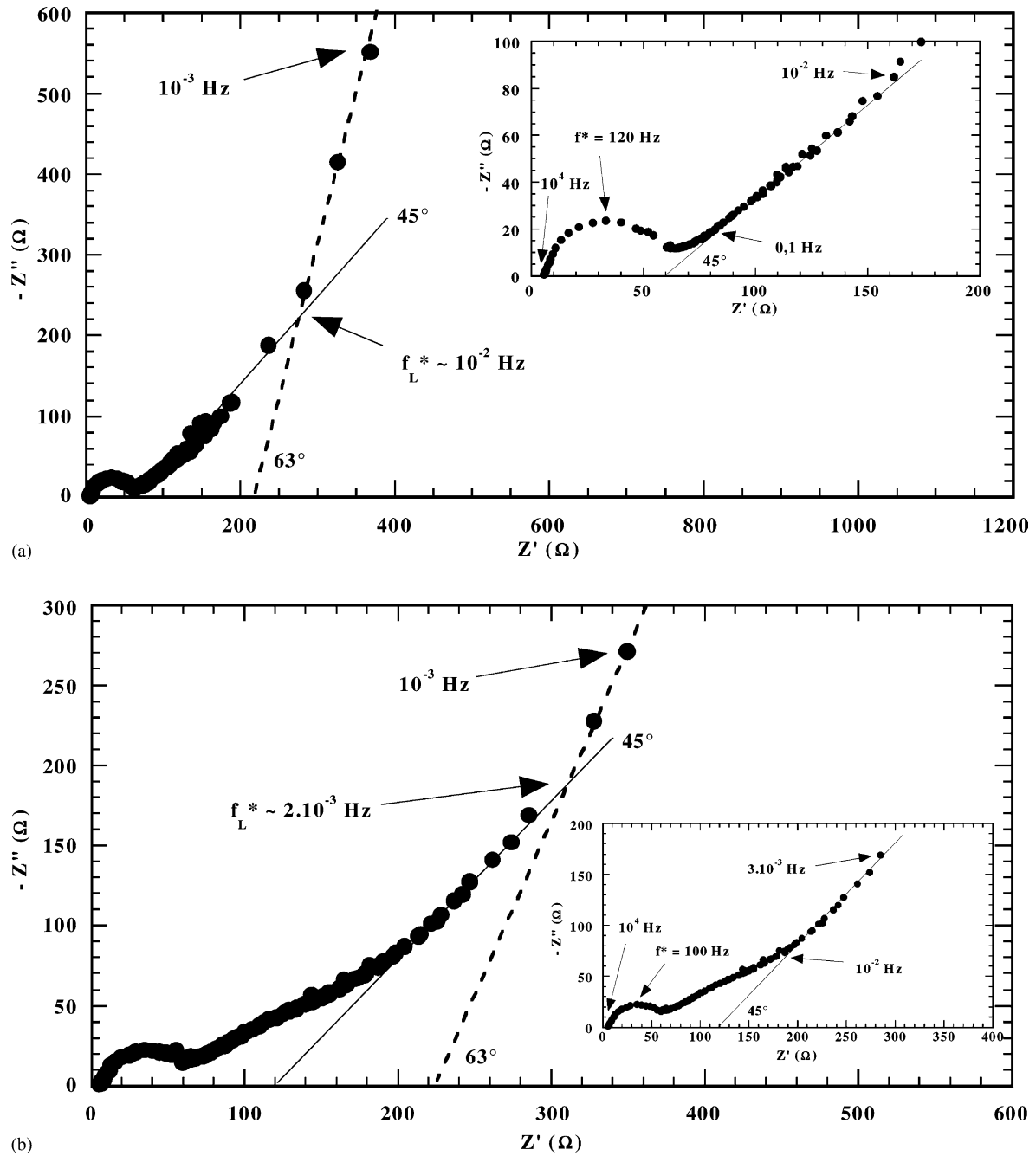
Fig. 9. Example of an ac impedance spectrum at $x = 0.2$ (a) corresponding to the compound $Li_{0.2}MnO_{1.84}\cdot0.6H_2O$. The ac impedance spectrum at $x = 0.6$; (b) corresponding to the compound $Li_{0.6}MnO_{1.84}\cdot0.6H_2O$. Determination of the slope A of the Warburg line for the calcul of D_{Li} with Eq. (7).

Table 2
Evolution of D_{Li} for SG birnessite and SG Co-birnessite at the first cycle and after the 10th cycle as a function of x

D_{Li} (cm^2 s^{-1})	SG birnessite first cycle	SG birnessite 10th cycle	SG Co-birnessite first cycle	SG Co-birnessite 10th cycle
$x = 0.1$	4×10^{-9}	1×10^{-11}	4×10^{-10}	3×10^{-10}
$x = 0.2$	1×10^{-9}	5×10^{-12}	1×10^{-10}	4×10^{-11}
$x = 0.3$	8×10^{-10}	2×10^{-13}	9×10^{-11}	8×10^{-12}
$x = 0.4$	7×10^{-11}	5×10^{-14}	8×10^{-11}	4×10^{-12}
$x = 0.5$	4×10^{-11}	3×10^{-15}	5×10^{-11}	1×10^{-12}
$x = 0.6$	4×10^{-11}		5×10^{-11}	

Calculation of the length for the diffusion pathway (L) from the limiting resistance (R_L) and capacitance (C_L) [36]:

$$\mathrm{Re}(Z_L) = R_L = \frac{V_M}{FS}\frac{dE}{dx}\frac{L}{3D_{Li}} \tag{8a}$$

$$-\mathrm{Im}(Z_L) = \frac{V_M}{FS}\frac{dE}{dx}\frac{1}{\omega L} = \frac{1}{\varpi C_L} \tag{8b}$$

as well as from the values of the frequency limit ($\varpi_L = 2D/L^2$) can be performed. L is found to be equal to $\approx 2\,\mu\mathrm{m}$. This is in good accord with the grain size evaluated from scanning microscopy experiments ($\varnothing_{\mathrm{particles}}$ # $2L$).

Then, an important point displayed by impedance spectroscopy is the possibility of accurately discriminating by frequencies the different rate-limiting processes. This is one of the reasons why the use of ac impedance spectroscopy is helpful and complementary to other techniques like the Basu and Worrel's method [28].

In order to check the consistency of kinetic data obtained for the $\mathrm{Li}_x\mathrm{MnO}_{1.84}\cdot 0.6\mathrm{H}_2\mathrm{O}$ electrode, we also applied the technique developed by Basu and Worrel. The CPRT method has been described in many studies devoted to cathodic materials, in particular for $\mathrm{V}_2\mathrm{O}_5$-based materials [37–39], $\mathrm{Nb}_2\mathrm{O}_5$ [40], WO_3 [41], TiS_2 [28] and NbSe_3 [42]. In this method, a pulse of current is generated on the electrode in order to create a concentration gradient Δx of lithium ions at the surface of the compound. After the current is switched off, the electrode potential recovers to its original value (Fig. 10a), if the amplitude and duration of the pulse are small enough to keep the composition of the cathode constant ($\Delta x \ll x$).

Fick's second equation for an instantaneous planar source of diffusing species in semi-infinite geometry ($t \ll L^2/D_{Li}$) yields to the evolution of the relaxation potential as a function of $t^{-1/2}$, from which the chemical diffusion coefficient D_{Li} is calculated:

$$D_{Li} = \left[\left(\frac{dE}{dt^{1/2}}\right)^{-1}\left(\frac{dE}{dx}\right)\left(\frac{I\tau V_M}{SF\pi^{1/2}}\right)\right]^2 \tag{9}$$

where, I, τ, V_M, S, F, and t are respectively, the intensities of the current pulse ($=200\,\mu\mathrm{A}$), the pulse duration ($=10\,\mathrm{s}$), the molar volume ($=25\,\mathrm{cm}^3\,\mathrm{mol}^{-1}$), the active surface area (cm^2), the Faraday constant, the time (s) and the half thickness (cm) of the material, since the electrolyte is in contact with both sides of the samples. ($dE/dt^{-1/2}$) is the slope of the straight line obtained from the evolution of the relaxation potential versus $t^{-1/2}$ (Fig. 10b).

Eq. (9) is relevant only if lithium diffusion is the rate-limiting process in the time range, which is not easy to determine. This domain of the time is known from the frequency range where the Warburg region is observed in ac impedance measurements. The two sets of data determined from ac impedance measurements and pulse relaxation experiments are compared and reported in Fig. 11.
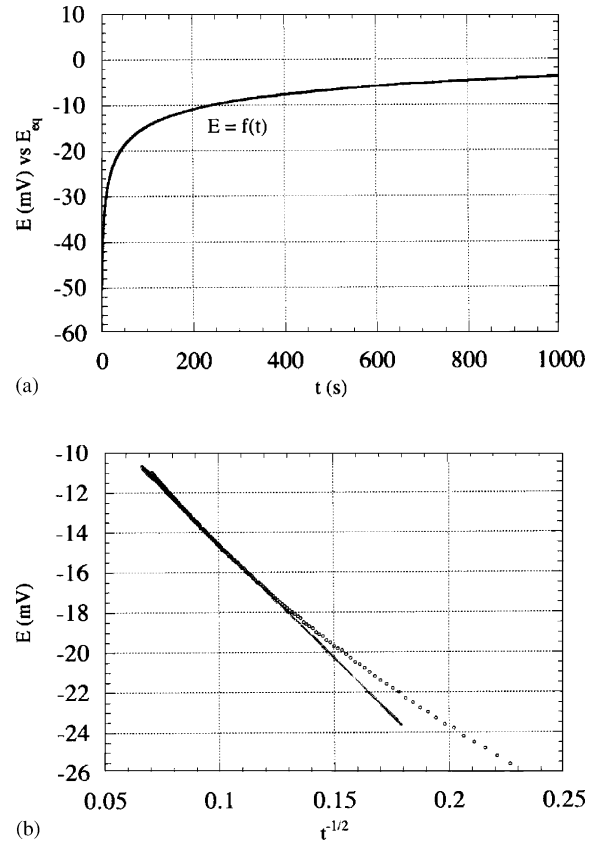

Fig. 10. (a) Example of a potential relaxation curve after current pulse imposition corresponding to the compound $\mathrm{Li}_{0.50}\mathrm{MnO}_{1.84}\cdot 0.6\mathrm{H}_2\mathrm{O}$; (b) $E = f\,(t^{-1/2})$. Determination of the slope for the calculated value of D_{Li} with Eq. (9).

The results show a good agreement within experimental errors between the two methods. Starting from a high value for $x = 0.025$, D_{Li} rapidly decreases and stabilizes between $0.15 < x < 0.3$ ($D_{Li} = 10^{-9}\,\mathrm{cm}^2\,\mathrm{s}^{-1}$). For higher x values, D_{Li} decreases by one order of magnitude around $10^{-10}\,\mathrm{cm}^2\,\mathrm{s}^{-1}$. For $x > 0.65$, D_{Li} is found to drop by two orders of magnitude to reach values as low as $2\times 10^{-13}\,\mathrm{cm}^2\,\mathrm{s}^{-1}$ for $x = 0.75$.
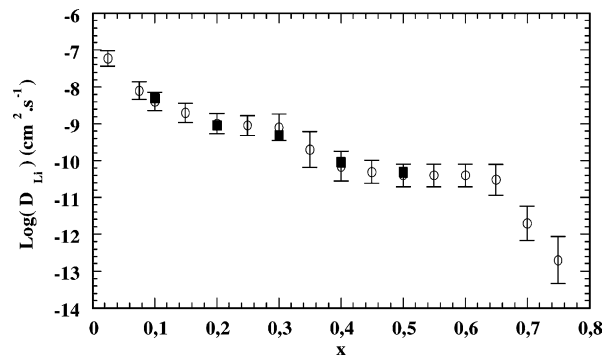

Fig. 11. Evolution of the chemical diffusion coefficient of lithium ions with the composition: ($\bigcirc$) determined by ac impedance spectroscopy measurements; ($\blacksquare$) determined by Basu & Worrel technic.
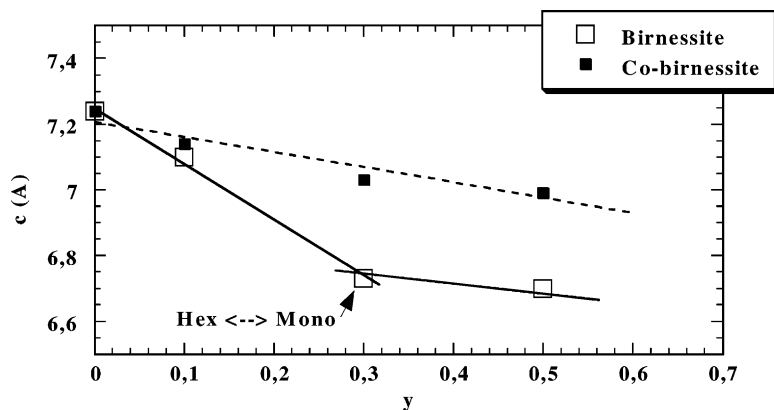
Fig. 12. Evolution of the interlayer spacing c for sol–gel birnessite ($\square$) (from [25]) and Co-birnessite ($\blacksquare$).

These results are consistent with kinetics of Li transport in various MnO_2 structures [43,44] with values around $10^{-10}\,cm^2\,s^{-1}$. Other measurements performed for other lamellar compounds shows similar values, $D_{Li} = 10^{-9}\,to\,10^{-11}\,cm^2\,s^{-1}$ for MoO_3 [45], $D_{Li} = 10^{-11}\,cm^2\,s^{-1}$ for V_2O_5 [46] and $D_{Li} = 10^{-9}$ to $5\times10^{-8}\,cm^2\,s^{-1}$ for TiS_2 [28].

From X-ray diffraction experiments performed on electrochemically lithiated samples, it is kwown that the c parameter decreases as Li insertion proceeds [25]. The host lattice significantly contracts in the Li composition range $0 < x < 0.3$, i.e. 7.5% along the c-axis, whereas for $0.3 < x < 0.7$ Li, accommodation induces a negligible change in the inter-layer space (Fig. 12). These data have been completed by XRD and TGA/DSC experiments performed on chemically lithiated samples [47]. The latter indicates an hexagonal-monoclinic distortion takes place with a two region phase for $0.1 < x \leq 0.2$ and a one phase region appears for $x > 0.2$ with no variation of the quantity of water during lithium insertion.

Due to the low Li content in birnessite, the high values of D_{Li} for $x < 0.1$ can be easily understood, while the small decrease of D_{Li} can be correlated with the continuous contraction of the interlayer spacing which is maximum for $x = 0.3$. The lower interlayer space of the monoclinic

region ($x > 0.3$) combined with the higher Li content makes the kinetics of Li transport slower for $x > 0.3$. The lack of structural data for Li rich compositions hinders any correlation.

The evolution of the specific capacity is reported as a function of cycle numbers at $C/20$ rate (Fig. 13). The trend in the cycling behavior of the SG birnessite is a strong decrease of the specific capacity from 230 to 170 mAh g^{-1} during the first ten cycles. It stabilizes around 170 mAh g^{-1} which corresponds to a faradaic yield of 0.6 F mol^{-1} showing the slow kinetics related to the highest Li contents ($x > 0.6$) hinders higher depths of discharge to be used. Second, a new but slow and constant capacity fading takes place after 20 cycles, to reach 155 mAh g^{-1} after 30 cycles.

In order to circumvent such a behavior, we recently reported the sol–gel synthesis of a Co-doped form [48] with the same hexagonal structure (Fig. 4b). The chemical formula of the Co-doped birnessite is $Mn_{0.85}Co_{0.15}O_{1.84}\cdot$ $0.6H_2O$ ($Z = 3.7$). As shown in Fig. 12, a constant value of the capacity (170 mAh g^{-1}) is obtained during all the cycling experiments, the cobalt ions being probably responsible for the better structural stability of the host lattice.

In order to get more information on the capacity fading of the SG birnessite, impedance measurements have been performed at different x values after 10 cycles. The values
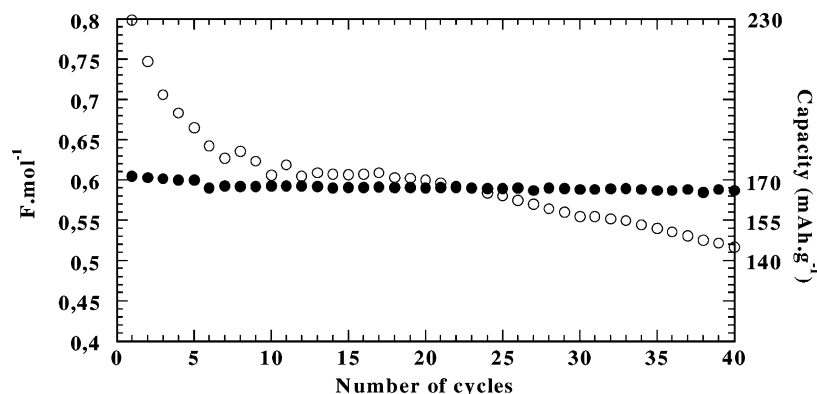

Fig. 13. Comparison of the evolution of the faradaic capacity with the number of cycles at $C/20$ for sol–gel birnessite ($\bigcirc$) and for sol–gel Co-birnessite ($\bullet$).

of the chemical diffusion coefficient D_{Li} summarized in Table 2 and calculated from the Warburg region at different state of discharge for cycles one and 10 clearly outline the poor kinetics of Li transport after cycling. Indeed, D_{Li} reaches the values much lower than $10^{-13}\,cm^2\,s^{-1}$ for $x > 0.3$ after 10 cycles. This has to be related with a strong disordering process evidenced by the XRD pattern reported in Fig. 14 where no defined diffraction line appears. The faster kinetics of Li transport in the Co-doped form tends to prove that Co ions are incorporated in MnO_2 sheets as Co^{3+} ions in substitution of manganese ions [49].

Comparison of the complex impedance diagram obtained for the SG birnessite and the Co-doped compounds in the frequency range 4×10^4 to 10^{-3} Hz for the first and the tenth cycle is summarized in Figs. 15 and 16. As far as the SG birnessite is concerned, an ill-defined charge transfer semi-circle appears as well as a Warburg region which still exists after 10 cycles in a frequency range translated towards lower values. Moreover, the cathode impedance greatly increases,
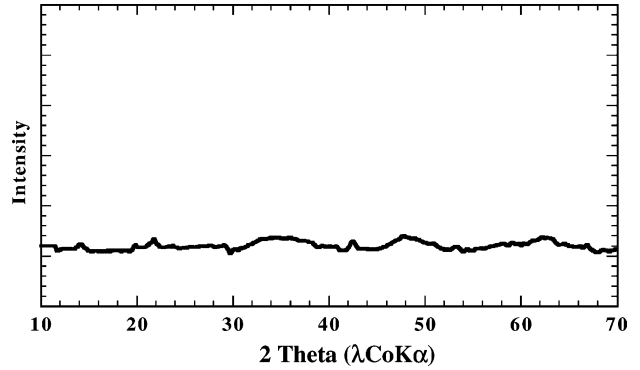

Fig. 14. XRD diffraction pattern of the sol–gel birnessite after 10 cycles (λ Co Kα).

in particular the resistance at low frequency increases at least by one order of magnitude. This behavior is well consistent with the poor cycle life of the compound due to large polarization observed in charge discharge curves. Conversely
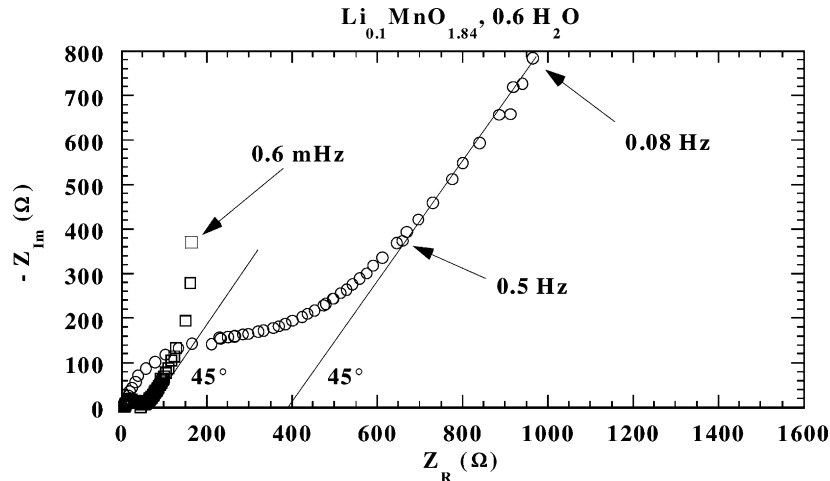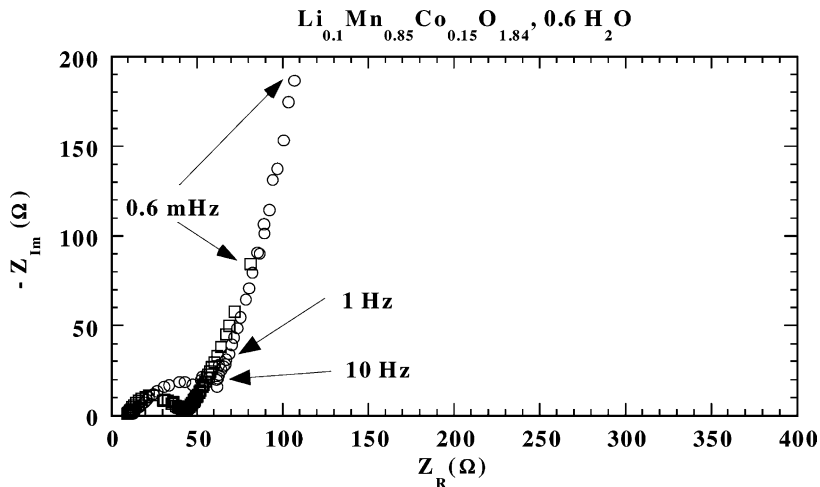

Fig. 15. Comparison of the ac complex impedance diagrams obtained in the frequency range 4×10^4 to 10^{-3} Hz for the first and the tenth cycle for sol–gel birnessite ($Li_{0.1}MnO_{1.84}\cdot0.6H_2O$).

Fig. 16. Comparison of the ac complex impedance diagrams obtained in the frequency range 4×10^4 to 10^{-3} Hz for the first and the tenth cycle for sol–gel Co-birnessite at the same lithium content ($Li_{0.1}Mn_{0.85}Co_{0.15}O_{1.84}\cdot0.6H_2O$).
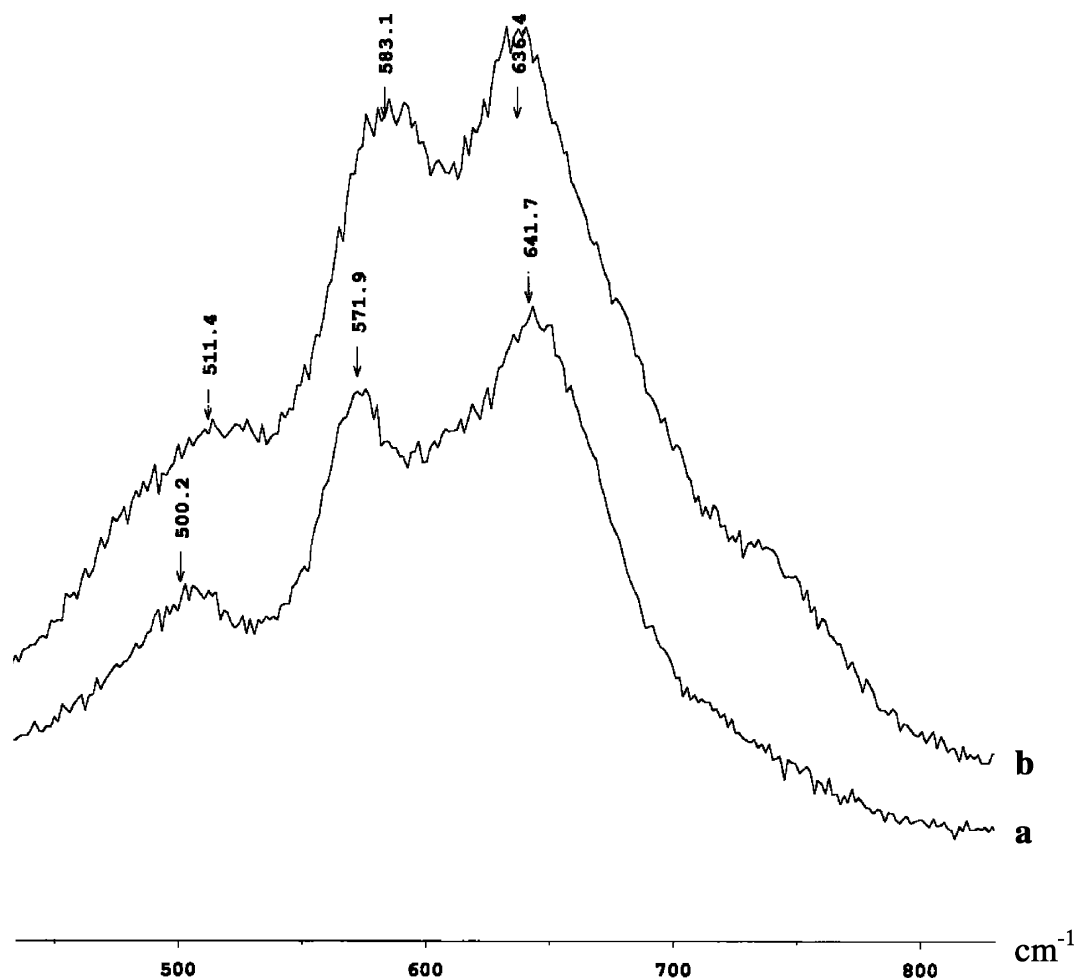
Fig. 17. RAMAN spectra of (a) $MnO_{1.84} \cdot 0.6H_2O$ and (b) $Mn_{0.85}Co_{0.15}O_{1.84} \cdot 0.6H_2O$.

for Co-doped oxide, no change is observed in the complex impedance diagram (Fig. 16) showing a constant structural and electrochemical response of the system, in terms of kinetics of Li transport in the oxide (Table 2), in good accord with the long cycle life exhibited by this compound.

The present cycling tests can be considered as promising when a comparison is made with published results on other birnessite materials. The best results recorded in the case of the dehydrated sodium phyllomanganates reported by Strobel et al. [32] do not exceed 100 mAh g^{-1} at low *C* rate after the third cycle in the voltage range 3.8–1.2 V. In other respects, attractive properties are obtained with the 2*D* dehydrated form of the prelithiated ranceite-type manganese oxide with a specific capacity of 200 mAh g^{-1} mentioned in the voltage range 4.3–2 V but after only 10 cycles [33].

In a few words, the cathode impedance of the Co-doped birnessite is 10 fold lower than that exhibited by the undoped birnessite which explains its better cycling behavior. We think the significant structural changes occurring when Li accommodation process into SG birnessite are probably responsible for important volume changes leading to the loss of electrochemical domains and then the occurrence of polarization.

In order to confirm this more important inner stability of the cobalt doped birnessite, we have performed measurements by mean of Raman spectroscopy on the sol–gel birnessite $MnO_{1.84} \cdot 0.6H_2O$ (Fig. 17a) and on the Co-birnessite (Fig. 17b).

These spectra have been obtained under a weak laser excitation power (120 μW) in order to aleviate any decomposition of the samples.

The Raman band at 642 cm^{-1} is usually attributed to the symmetric stretching vibration n(Mn–O) of the [MnO$_6$] groups [50]. It corresponds to the symmetry mode A$_{1g}$ from spectroscopic space group O$_h^7$. The band located at 572 cm^{-1} corresponds to the stretching symmetry mode F$_{2g}$. This one is particularly strong in our case, compared with the literature data related to lithiated spinel, which is significant with the high rate of Mn(IV) in our compounds. The Raman spectrum of Co-birnessite have the same characteristics, in the frequency range 400–800 cm^{-1}. The most important change is observed on the frequency attributed to the stretching mode T$_{2g}$ which presents here a shift of 12 cm^{-1} towards high frequencies. This result indicates a strengthening of the Mn–O bond in the cobalt doped birnessite and evidences the stronger network energy of this material.
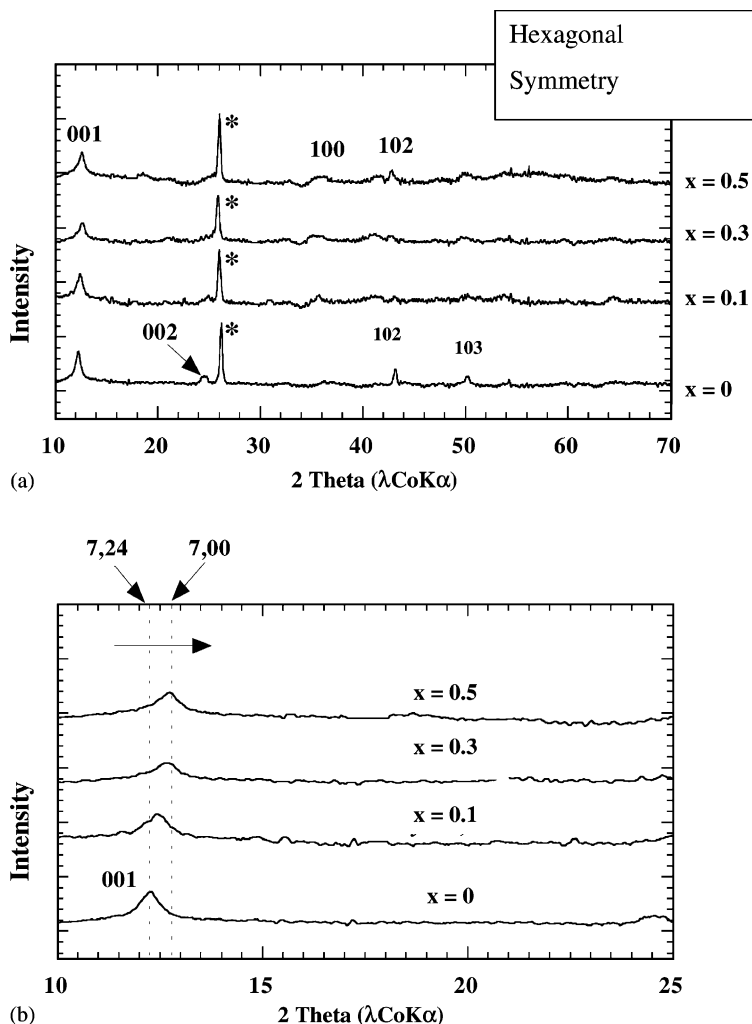
Fig. 18. X-ray diffraction pattern (λ Co Kα) of (a) Co-birnessite in function of the intercalation rate, *x*, of lithium, (b) zoom on the 10–25° part (2*θ*); ∗ diffraction peak of graphite.

X-ray diffraction experiments have also been performed onto the Co-birnessite in function of the intercalation rate of lithium (Fig. 18). First, we have not observed an hexagonal-monoclinic distortion. Second, even when a similar effect has been previously recorded for Li accommodation in undoped sol–gel birnessite, the order of magnitude for the *c* variation versus *x* is much lower in the case of Li insertion in the cobalt birnessite (Fig. 12). We observe a decrease of the *c* parameter as lithium insertion occurs in $Li_xCo_{0.15}Mn_{0.85}O_{1.84} \cdot 0.6H_2O$ ($c = 7.24$ Å for $x = 0$; $c = 7.0$ Å for $x = 0.5$) of 3%, whereas a contraction of 7.5% is obtained in the case of $Li_xMnO_{1.84} \cdot 0.6H_2O$ ($c = 7.24$ Å for $x = 0$; $c = 6.70$ Å for $x = 0.5$).

Our results in terms of rechargeable capacity and cycle life for the Co-birnessite are then interesting as compared in the case of undoped-birnessite. This work ascertains that water is stable as lithium insertion proceeds and the benefic role of cobalt. Hence, this layered hydrated Co-birnessite can be considered with interest for practical use in rechargeable 3 V lithium batteries.

References

[1] M.M. Thackeray, W.I.F. David, P.G. Bruce, J.B. Goodenough, Mater. Res. Bull. 18 (1983) 4611.

[2] T. Ohzuku, M. Kitagawa, T. Hirai, J. Electrochem. Soc. 137 (1990) 769.

[3] J.M. Tarascon, E. Wang, F.K. Shokoohi, W.R.Mc. Kinnon, S. Colson, J. Electrochem. Soc. 138 (1991) 2859.

[4] P.M. De Wolff, Acta Cryst. 12 (1959) 341.

[5] S. Sarciaux, A. Le Gal La Salle, A. Verbaere, Y. Piffard, D. Guyomard, J. Power Sources 81/82 (1999) 656.

[6] T. Nohma, T. Saito, N. Furukawa, H. Ikeda, J. Power Sources 26 (1989) 389.

[7] T. Nohma, Y. Yamamoto, K. Nishio, I. Nakane, N. Furukawa, J. Power Sources 32 (1990) 373.

[8] L. Li, G. Pistoia, Solid State Ionics 47 (1991) 231.

[9] J.M. Tarascon, W.R. McKinnon, F. Coowar, T.N. Bowmer, G. Amatucci, D. Guyomard, J. Electrochem. Soc. 141 (1994) 1421.

[10] C. Masquelier, M. Tabuchi, K. Ado, R. Kanno, Y. Kobayashi, Y. Maki, O. Nakamura, J.B. Goodenough, J. Solid State Chem. 123 (1996) 255.

[11] T. Tsumura, A. Shimizu, M. Inagaki, Solid State Ionics 90 (1996) 197.

[12] R.J. Gummow, A de Kock, M.M. Thackeray, Solid State Ionics 69 (1994) 59.

[13] A. Yamada, K. Miura, K. Hinokuma, M. Tanaka, J. Electrochem. Soc. 142 (1995) 2149.

[14] J.B. Goodenough, M.M. Thackeray, W.I.F. David, P.G. Bruce, Rev. Chim. Miner. 21 (1984) 435.

[15] W.I.F. David, M.M. Thackeray, L.A. de Piciotto, J.B. Goodenough, J. Solid State Chem. 67 (1987) 316.

[16] D.H. Jang, S.M. Oh, J. Electrochem. Soc. 144 (1997) 3342.

[17] K. Nishimura, T. Douzono, M. Kasai, H. Andou, Y. Murakana, Y. Kozono, J. Power Sources 81/82 (1999) 420.

[18] M. Morita, O. Yamada, M. Ishikawa, J. Power Sources 81/82 (1999) 425.

[19] C. Sigala, D. Guyomard, A. Verbaere, Y. Piffard, M. Tournoux, Solid State Ionics 81 (1995) 167.

[20] C.J. Brinker, G.W. Scherer, in Sol–Gel Science. Academic Press, San Diego, 1990.

[21] J. Livage, F. Beteille, C. Roux, M. Chatry, P. Davidson, Acta Mater. 46 (1998) 743.

[22] J.P. Pereira-Ramos, S. Bach, N. Baffier, R. Messina, Solid State Ionics 40/41 (1990) 974.

[23] S. Bach, M. Henry, N. Baffier, J. Livage, J. Solid State Chem. 88 (1990) 325.

[24] S. Bach, J.P. Pereira-Ramos, N. Baffier, J. Power Sources 81/82 (1999) 273.

[25] S. Bach, J.P. Pereira-Ramos, N. Baffier, Electrochem. Acta 36 (1991) 1595.

[26] S. Bach, J.P. Pereira-Ramos, N. Baffier, J. Electrochem. Soc. 143 (1996) 3429.

[27] J.P. Pereira-Ramos, N. Baffier, in: G. Pistoia (Ed.), Lithium Batteries, New Materials, Developments and Perspectives, Elsevier, North Holland, 1994.

[28] S. Basu, W.L. Worrell, in: Vashita, Mundy, Shenoy (Eds.), Fast Ion Transport in Solids, Elsevier, North Holland, 1979, p. 149.

[29] M.J. Katz, R.C. Clarke, W.F. Nye, Anal. Chem. 28 (1956) 1956.

[30] E. Stähli, in Uber Manganate (IV) mit Schichten-Struktur., Ph.D. Dissertation, University of Bern, Switerland, 1968.

[31] R. Giovanoli, E. Stähli, W. Feitknecht, Helv. Chim. Acta 53 (1970) 453.

[32] P. Strobel, C. Mouget, Mater. Res. Bull. 28 (1993) 93.

[33] F. Leroux, D. Guyomard, Y. Piffard, Solid State Ionics 80 (1995) 299.

[34] D.C. Golden, J.B. Dixon, C.C. Chen, Clays Clay Miner. 34 (1986) 511.

[35] R. Chen, P. Zavalij, M.S. Whittingham, Chem. Mater. 8 (1996) 1275.

[36] C. Ho, I.D. Raistrick, R.A. Huggins, J. Electrochem. Soc. 127 (2) (1980) 343.

[37] J.P. Pereira-Ramos, R. Messina, J. Perichon, Solid State Ionics 15 (1985) 173.

[38] S. Bach, J.P. Pereira-Ramos, N. Baffier, R. Messina, J. Electrochem. Soc. 137 (1990) 1042.

[39] R. Baddour-Hadjean, J. Farcy, J.P. Pereira-Ramos, N. Baffier, J. Electrochem. Soc. 143 (1996) 2083.

[40] N. Kumagai, I. Ishiyama, K. Tanno, J. Power Sources 20 (1987) 193.

[41] B. Reichman, A.J. Bard, J. Electrochem. Soc. 126 (1979) 583.

[42] B.V. Ratnakumar, G. Nagasubramanian, S. Di Stefano, C.P. Bankston, J. Electrochem. Soc. 139 (1992) 1513.

[43] P.G. Dickens, G.F. Reynolds, Solid State Ionics 5 (1981) 331.

[44] J. Vondrak, I. Jazubec, J. Bludska, J. Power Sources 14 (1985) 141.

[45] J.O. Besenhard, J. Heydecke, E. Wudy, H.P. Fritz, Solid State Ionics 8 (1983) 61.

[46] J. Farcy, R. Messina, J. Perichon, J. Electrochem. Soc. 137 (1990) 1337.

[47] P. Le Goff, S. Bach, J.P. Pereira-Ramos, N. Baffier, J. Mater. Chem. 4 (1994) 133.

[48] S. Franger, S. Bach, J.P. Pereira-Ramos, N. Baffier, Ionics 6 (2000) 470.

[49] A. Manceau, V.A. Drits, E. Silvester, C. Bartoli, B. Lanson, Am. Miner. 82 (1997) 1150.

[50] C. Julien, in: Materials for Li-ion batteries, NATO Science Series 3/85 (2000) 309.